An Energy-Efficient Antenna Impedance Detection Using Electrical Balance for Single-Step On-Chip Tunable Matching in Wearable/Implantable Applications

Minyoung Song, *Member, IEEE*, Chuang Lu, Ao Ba, Xiaoyan Wang, Yao-Hong Liu, *Member, IEEE*, Kenichi Shibata, Christian Bachmann, Kathleen Philips, *Member, IEEE*

***Abstract*— A low-power impedance detection method using a hybrid transformer and its analysis are presented. A balun is reused for the hybrid transformer to achieve area-efficiency. The complex impedance detection enables faster optimization on a tunable matching network and its calibration technique increases the detection accuracy. The proposed impedance detection method fabricated in a 40-nm CMOS process consumes only 0.83 mW and demonstrates the accuracy of less than 18° and 0.1 on the Γ detection up to $|\Gamma_{Ant}|$ of 0.5 in ISM2.4 GHz band. After single-step matching network tuning, PA power and RX noise figure are improved by up to 1.2 dB and 1.3 dB, respectively.**

***Index Terms*—Antenna impedance detection, impedance matching, tunable circuits and devices, hybrid transformer, electrical balancing, CMOS process.**

I. Introduction

Wearable/implantable devices, e.g., heart-rate-monitor straps [1] and implanted wireless sensors, e.g., capsule endoscopy [2] need a fully integrated adaptive front-end with a tunable matching network (TMN) using low-power and fast impedance detection, since they consume ultra-low-power (ULP) and require robust and efficient operation. One of the most challengeable issues is the antenna proximity effect, which can significantly degrade the antenna and front-end performance and hence battery lifetime [3]. In order to reduce the antenna impedance mismatch caused by the proximity effect, adaptive TMNs [4]-[11] are required to improve the RF frontend performance. The impedance mismatch detection is crucial in such tuning systems in terms of tuning speed and power consumption. The adaptive TMN can be implemented by directional coupler [4], [5], quarter-wave transmission line [6] or off-chip tuner [8] to detect the antenna impedance. However, those approaches need external components, which increase cost and form factor, thus are not suitable for wearable/implantable devices. Further, all of them have also limited detection precision, and only detect the mismatched impedance in certain direction [5],[7] or range [8]. Yet, no on-chip exact impedance detection has been demonstrated. In addition, the external detection methods [5], [8] consume approximately 30mW due to the complexity of the detection circuits, which is not suitable for the ULP applications with only a sub-mW power budget for the detection circuit. A fully integrated antenna impedance detection has been realized with RF amplitude detection [9], [10]. The amplitude detection method can be designed in simple structure and easy to integrate. However, since phase information of the antenna impedance is not detected, a blind search is preceded to achieve accurate impedance detection. The blind search to find the phase information requires extra time-consuming optimization methods (i.e. exhaustive search or a successive approximation), which increases complexity and current consumption.

In this work, a fully integrated low-power impedance-detection technique is presented for low power transceiver front-ends [11]. In order to reduce 2nd harmonic distortion of the PA mode, modern transceiver front-ends [12]-[14] adopt balun transformer to convert differential signals to a single-ended one. The detection technique reuses the balun transformer as a hybrid transformer. Therefore, the impedance-detection technique is area-efficient without degrading performance. The hybrid transformer detects a "leakage signal" due to the impedance mismatch between the actual load impedance and an on-chip reference load. The proposed detected signal down converter extracts the I and Q information which gives both amplitude and phase information of the antenna impedance. Additionally, the proposed impedance calibration technique improves a detection precision and enables a single-step fast matching-network tuning.

This paper is organized as follows. The hybrid transformer based impedance detection technique is introduced in Section II. The overall circuit implementation is discussed in Section III. Section IV presents the measurement results and the die photo, implemented in 40-nm CMOS process. Finally, conclusion is drawn in Section V.

M. Song, A. Ba, X. Wang, Y-.H. Liu, C. Bachmann and K. Philips are with the IMEC-Holst Centre, Eindhoven, The Netherlands (e-mail: Minyoung.Song@imec-nl.nl).

C. Lu, was with IMEC-Holst Centre, Eindhoven, The Netherlands. He is now with the NXP, Eindhoven, The Netherlands.

K. Shibata is with Renesas Electronics Corporation, Tokyo, Japan.

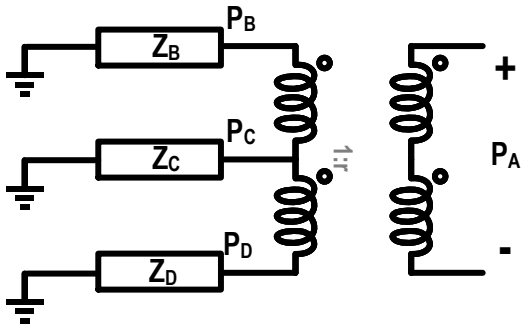

Fig. 1. Hybrid transformer [15].

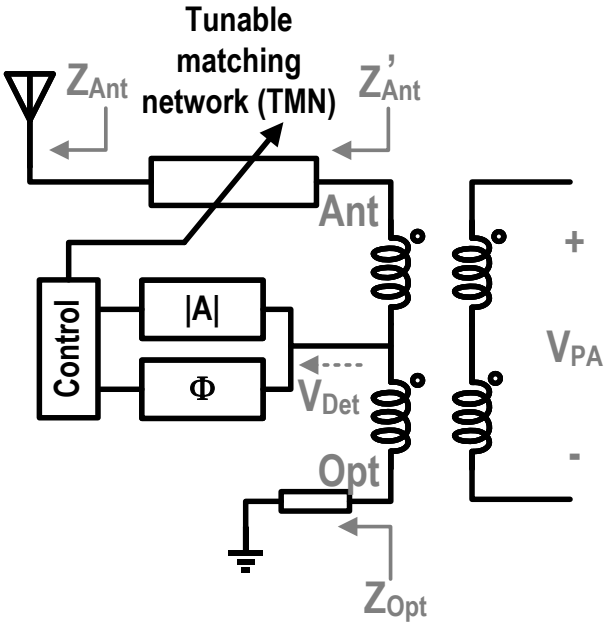

Fig. 2. Conceptual diagram of the antenna-impedance detection.

II. Impedance Detection using Hybrid Transformer

A hybrid transformer has been traditionally used in the telephone plant [15]. The hybrid transformer is a five port passive component as shown in Fig. 1. The three ports of the primary coil connect to P_B, P_C and P_D, and the two ports of the secondary coil connect to the differential P_A. An useful characteristic of the hybrid transformer is its bi-conjugacy. i. e., if impedances at P_B and P_D are matched, no signal from P_A appears at P_C (isolated). By virtue of the characteristic, The hybrid transformer has been used for duplexer [16]-[18] to achieve a high TX-RX isolation by satisfying an electrical balance. In this work, the hybrid transformer is utilized in a different configuration for the impedance detection. In the primary coil, a detection port is tapped at a ratio of 1:r, as shown in Fig. 1. Assume r=1, in which case the detection port is the center tap of the primary coil, if the load impedance at P_B equals the load impedance P_D, i. e. $Z_B = Z_D$, the signal from the differential P_A will be coupled to the primary coil, and no signal current will flow into the detection port, P_C, as a common mode port. As Z_D deviates more from Z_B, the power that goes into the detection port (i.e., P_C) will be higher.

The concept of the proposed detection technique using a hybrid transformer is shown in Fig. 2..The actual impedance seen from the transformer (i.e. Z'_{Ant} or Γ'_{Ant}) is compared to the desired optimum reference impedance (Z_{Opt}), and the amplitude and phase of the detected "leakage" signal ($\overrightarrow{V_{Det}}$) is utilized to determine the antenna impedance.

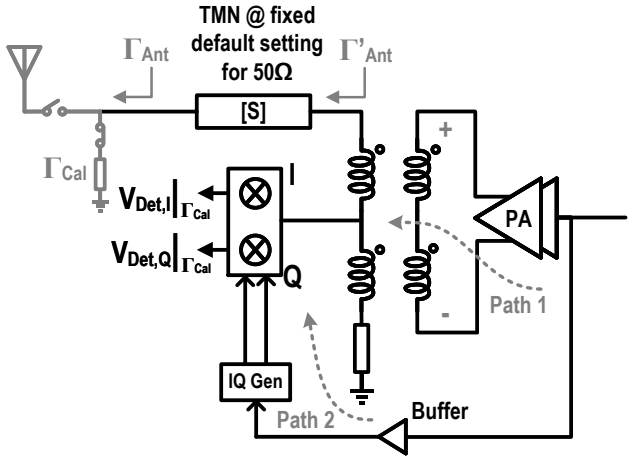

Fig. 3. Calibration scheme of the antenna-impedance detection.

The ideal S-matrix of the hybrid transformer in Fig. 2 can be defined as [17]

$$\begin{bmatrix} b_{Det} \\ b_{PA} \\ b_{Ant} \\ b_{Opt} \end{bmatrix} = \frac{1}{\sqrt{1+r}} \begin{bmatrix} 0 & 0 & \sqrt{r} & 1 \\ 0 & 0 & 1 & -\sqrt{r} \\ \sqrt{r} & 1 & 0 & 0 \\ 1 & -\sqrt{r} & 0 & 0 \end{bmatrix} \begin{bmatrix} a_{Det} \\ a_{PA} \\ a_{Ant} \\ a_{Opt} \end{bmatrix} \quad (1),$$

where a_{Det}, a_{PA}, a_{Ant}, a_{Opt}, b_{Det}, b_{PA}, b_{Ant} and b_{Opt}, are incident and reflected power waves at each nodes (Ant, Det, PA and Opt).

To calculate the relation between $\overrightarrow{V_{Det}}$ and $\overrightarrow{V_{PA}}$, b_{Det} is derived from the S-matrix as

$$b_{Det} = \sqrt{\frac{r}{1+r}} \cdot a_{Ant} + \sqrt{\frac{1}{1+r}} \cdot a_{Opt} \quad (2).$$

Since the energy from PA is only considered to calculate the relation,.b_{Ant} and b_{Opt} can be simplified as

$$b_{Ant} = \sqrt{\frac{r}{1+r}} \cdot a_{Ant} + \sqrt{\frac{1}{1+r}} \cdot a_{PA} = \sqrt{\frac{1}{1+r}} \cdot a_{PA} \quad (3).$$

$$b_{Opt} = \sqrt{\frac{1}{1+r}} \cdot a_{Det} - \sqrt{\frac{r}{1+r}} \cdot a_{PA} = -\sqrt{\frac{r}{1+r}} \cdot a_{PA} \quad (4).$$

a_{Ant} and a_{Opt} can be also calculated as

$$a_{Ant} = \sqrt{\frac{1}{1+r}} \cdot \Gamma'_{Ant} \cdot a_{PA} \quad (5),$$

$$a_{Opt} = -\sqrt{\frac{r}{1+r}} \cdot \Gamma_{Opt} \cdot a_{PA} \quad (6),$$

where Γ'_{Ant} and Γ_{Opt} are reflection coefficients from Ant and Opt nodes,

$$\Gamma'_{Ant} = \frac{a_{Ant}}{b_{Ant}} = \frac{Z'_{Ant} - R_o}{Z'_{Ant} + R_o} \quad (7),$$

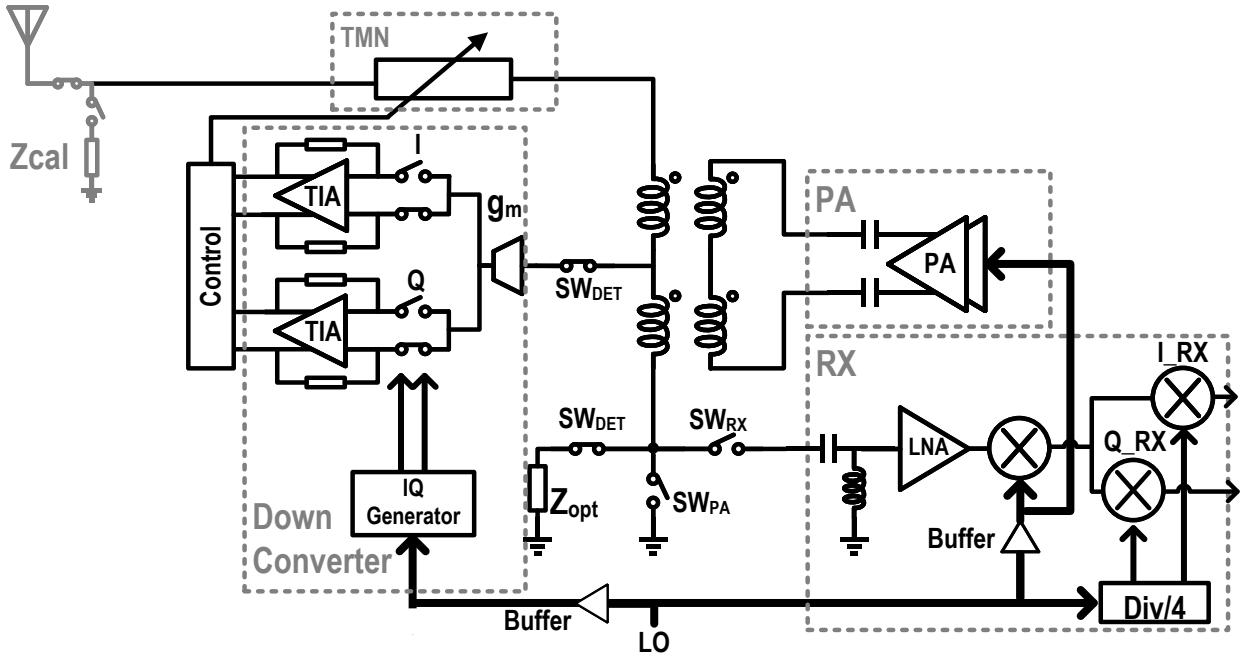

Fig. 4. Top-level diagram of the front-end module for impedance mismatch detection and tuning.

$$\Gamma'_{Opt} = \frac{a_{Opt}}{b_{Opt}} = \frac{Z_{Opt} - rR_o}{Z_{Opt} + rR_o} \tag{8}$$

R_o is 50Ω in this case and Opt node is matched when Z_{Opt} is equal to rRo [15].

Thus, the relation between $\overrightarrow{V_{Det}}$ and $\overrightarrow{V_{PA}}$ is

$$\frac{\overrightarrow{V_{Det}}}{\overrightarrow{V_{PA}}} = \frac{\sqrt{r}}{1+r} \cdot \left(\Gamma'_{Ant} - \Gamma_{Opt}\right) \tag{9}$$

$$\frac{\overrightarrow{V_{Det}}}{\overrightarrow{V_{PA}}} = \frac{\sqrt{r}}{1+r} \cdot \left(\Gamma'_{Ant}\right) \tag{10}$$

where Opt node is matched.

As (10), when Z_{Opt} of 8Ω ($rR_o = 0.16 \cdot 50 = 8\Omega$) is loaded, the phase difference between $\overrightarrow{V_{Det}}$ and $\overrightarrow{V_{PA}}$ reveals the phase of Γ'_{Ant}, and the ratio of the amplitude of $\overrightarrow{V_{Det}}$ over $\overrightarrow{V_{PA}}$ is the amplitude of Γ'_{Ant} multiplied by a constant depending on r, which is the aspect ratio of the transformer.

The impedance detection is done by an IQ down-conversion, as shown in Fig. 3, which preserves both amplitude and phase information. The switching signal of the IQ mixers is generated by the IQ generation. Note that the phase information of the IQ-mixer outputs (i.e. $\tan^{-1}(V_{Det,Q}/V_{Det,I})$) includes not only the phase of Γ'_{Ant}, but also phase offsets (φ_{offset}) introduced by the PA, the transformer, IQ generation, and the buffer. To improve the precision of Γ_{Ant} detection, an impedance calibration is necessary to de-embed the following parameters:

1) The phase offset φ_{offset}.

2) The absolute gain of the detection path

3) The impedance transformation of the 50Ω TMN (i.e. from Γ_{Ant} to Γ'_{Ant}).

$$\Gamma'_{Ant} = s_{22} - \frac{s_{12} \cdot s_{21} \cdot \Gamma_{Ant}}{1 - s_{11} \cdot \Gamma_{Ant}} \tag{11}$$

where S_{11},S_{12} and S_{21} are s-parameters of TMN. If the TMN has 50Ω of characteristic impedance i.e. $|S_{11}| \to 0$ and $|S_{22}| \to 0$,

$$\Gamma'_{Ant} = s_{12} \cdot s_{21} \cdot \Gamma_{Ant} \tag{12}$$

Therefore, in practice, $\overrightarrow{V_{Det}}$ can be redefined as

$$\begin{aligned} \overrightarrow{V_{Det}} &= \overrightarrow{V_{PA}} \cdot \left(A \cdot e^{j\phi_{offset}}\right) \cdot \frac{\sqrt{r}}{r+1} \cdot \Gamma'_{Ant} \\ &= \overrightarrow{V_{PA}} \cdot \left(A \cdot e^{j\phi_{offset}}\right) \cdot (s_{12} \cdot s_{21}) \frac{\sqrt{r}}{r+1} \cdot \Gamma_{Ant} \\ &= \overrightarrow{F_{Cal}} \cdot \Gamma_{Ant} \end{aligned} \tag{13}$$

where φ_{offset} is due to the phase offsets between path 1 and path 2, A is the gain of path 1.

$\overrightarrow{F_{Cal}}$ in (13) is necessary to be characterized to accurately derive Γ_{Ant} from $\overrightarrow{V_{Det}}$. $\overrightarrow{F_{Cal}}$ is characterized through a calibration scheme by shunting to a known (mismatched) impedance at the TMN input. In this condition, the I and Q outputs of the detection circuit are $V_{Det,I}|_{Cal}$ and $V_{Det,Q}|_{Cal}$. Thus, $\overrightarrow{F_{Cal}}$ is

$$\overrightarrow{F_{Cal}} = \frac{\overrightarrow{V_{Det|Cal}}}{\Gamma_{Cal}} = \frac{V_{Det,I|Cal} + j \cdot V_{Det,Q|Cal}}{\Gamma_{Cal}} \tag{14}$$

Then, the actual detected antenna reflection coefficient after calibration can be written as

$$\overrightarrow{\Gamma_{Det}} = \frac{\overrightarrow{V_{Det}}}{\overrightarrow{F_{Cal}}} = \frac{\left(V_{Det,I} + j \cdot V_{Det,Q}\right) \cdot \Gamma_{Cal}}{V_{Det,I|Cal} + j \cdot V_{Det,Q|Cal}} \tag{15}$$

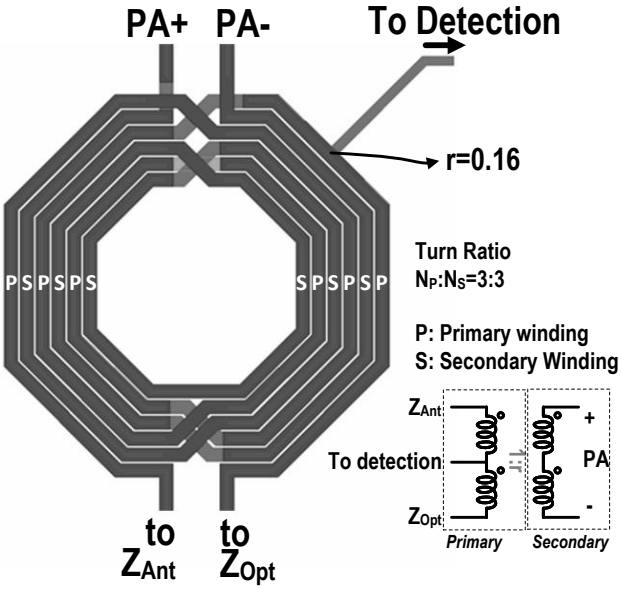

Fig. 5. Top view layout of the hybrid transformer.

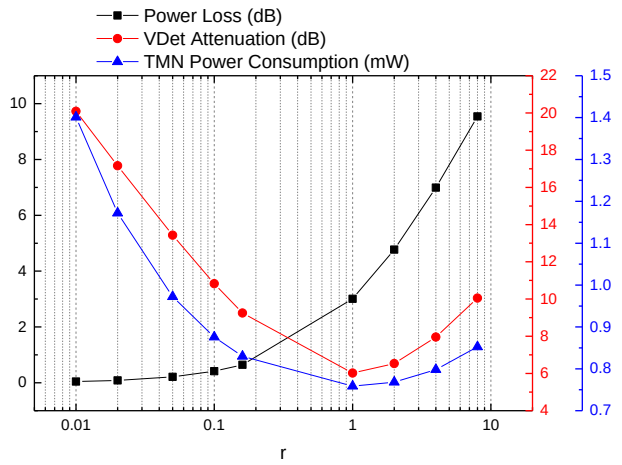

Fig. 6. Trade-off of hybrid transformer: Power loss at the Opt load, V_{Det} attenuation and power consumption of TMN.

TABLE I
SIMULATED INDUCTANCE VALUES AND QUALITY FACTORS OF HYBRID TRANSFORMER

@2.4 GHz	Inductance (nH)	Quality Factor
Primary (Z_{Ant}, Z_{Opt})	3.5	9.3
Secondary (PA+, PA-)	2.9	10.2
Coupling Coefficient	0.85	

The impedance calibration is done by switching to a reference impedance with a known Γ_{Cal} (e.g.,Γ_{Cal} of 0.5, or Z_{Cal} of 150Ω, is used in this design) at the antenna port. As shown in (15), the ratio between the known Γ_{Cal} and the corresponding detected IQ levels ($V_{Det,I}|_{Cal}$ + j·$V_{Det,Q}|_{Cal}$) is used to derive the actual Γ_{Det}. Note that the proposed calibration technique focuses on calibrating path-dependent parameters since those parameters are the major contributors on the proposed impedance detection precision. Non-path dependent parameters, e. g. load impedance dependence in PA, can also affect the detection precision.

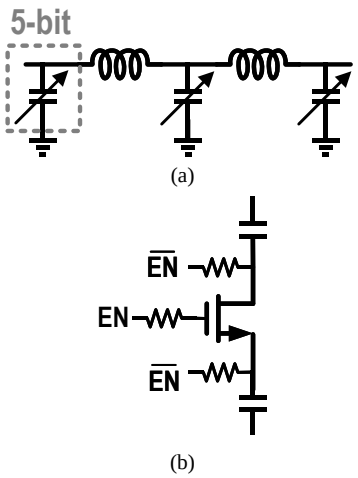

Fig. 7. (a) Two-stage pi-LC tunable matching network. (b) Unit cell of the switchable capacitor.

III. CIRCUIT IMPLEMENTATION

A. Overall Architecture

Fig. 4 shows the implemented top-level diagram. A front-end module that comprises PA and RX is integrated to estimate the performance of the impedance detection technique. A sliding-IF architecture is adopted for the RX since it is suitable for ULP applications, e.g., wearable/implantable devices. The balun for the differential PA is reused for the hybrid transformer, with an extra tap to the detection circuits. A TMN with a two-stage PI network is implemented with a tuning range to cover $|\Gamma_{Ant}|$ of up to 0.5. The down-converter converts the signal at the detection port of the hybrid transformer for a complex impedance detection. Furthermore, switches SW_{DET}, SW_{PA} and SW_{RX} select between a detection mode, a PA mode (hybrid transformer as a normal balun), and an RX mode. The control block would comprise a simple ADC, processor and memory. Since the control block can operate at system clock (normally, tens of MHz of crystal oscillator), its power consumption is relatively negligible compared to other detection circuits. Moreover, the proposed TMN only operates in the detection mode. Therefore, the power consumption of the control block does not contribute in the normal operation mode.

B. Hybrid Transformer

Comparing to the detector using weak coupling in [9], the hybrid transformer is more reliable, because its behavior is better controlled and less vulnerable to undesired coupling (e.g., EM coupling from the LC-tank of an oscillator). The transformer has an additional output power loss at the Opt load, which depends on the aspect ratio, r, as [17]

$$P_{LOSS} = 10\log_{10}(1+r) \quad (16).$$

However, as explained in (10), the mismatch detection capability is also degraded since the detection signal level is curtailed by low r (r <1). Therefore, the power consumption of the impedance detection part should be increased at low r. Considering the trade-off between loss and power consumption,

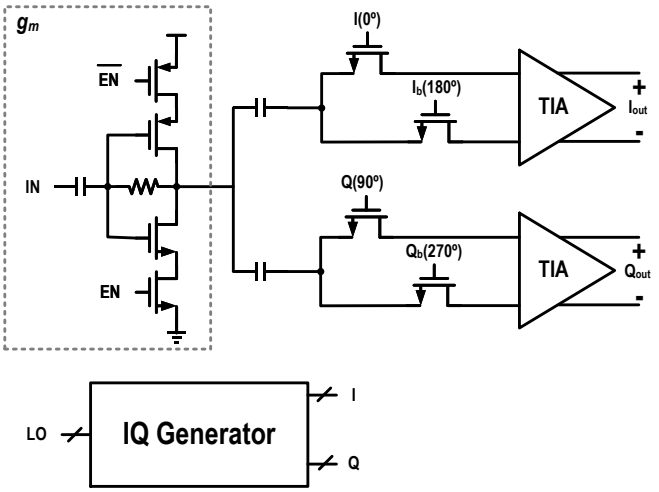

Fig. 8. Detected signal down converter for the impedance mismatch detection.

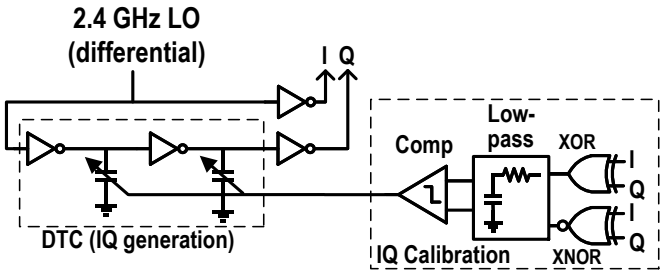

Fig. 9. DTC-based IQ generator and its calibration using XOR and XNOR.

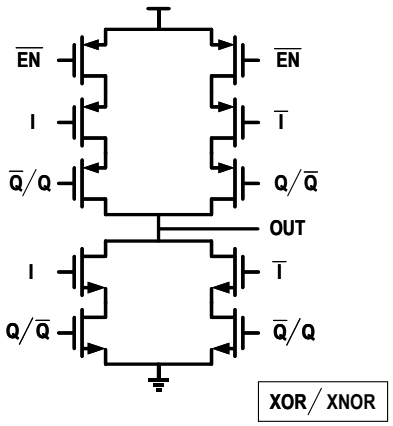

Fig. 10. Circuit diagram of the symmetrical XOR and XNOR.

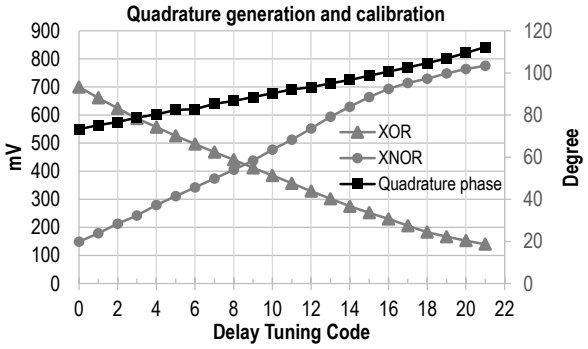

Fig. 11. DC values of XOR and XNOR and quadrature phase difference versus delay tuning code

r is set to 0.16 to achieve sub-mW of power consumption. When r = 0.16, the power loss at the reference load is about 0.6 dB and the proposed TMN dissipates 0.83 mW as illustrated in Fig. 6. As shown in Fig. 5, the transformer has 3-turn-to-3-turn ratio. The detection port lies at the position close to the Z_{Opt} port, to achieve r = 0.16. The simulated inductance values and coupling factor are listed in Table I.

C. Tunable Matching Network

The tuning capability is achieved from the shunt switchable capacitor banks, as shown in Fig. 7, which has lower loss and better linearity than series tunable capacitors. The TMN is characterized to map a setting for the optimum PA and LNA performance to each of the Γ_{Ant} values. Note that the passive components in the TMN are less sensitive to the temperature and supply, as a result of which frequent impedance calibration is not necessary. The TMN is sensitive to variations of the capacitors, which can be characterized in practice and applied to the default look-up-table (LUT). The detailed tuning method is described in Section IV.

D. Detected Signal Down Converter

The signal level at the detection port is converted by the proposed down converter as shown in Fig. 8. The down converter includes a trans-conductance stage (g_m), with a high impedance at the input and to provide the voltage to current conversion. I and Q passive mixers, trans-impedance amplifiers (TIAs) and IQ generator are followed. The g_m stage is a self-biased inverter, with switch transistor at the sources of the PMOS and NMOS, and is also possible to disable the g_m when the detection is not necessary. The TIA further convert the current into voltage afterwards. IQ generator produces the quadrature signals for the mixer. The detailed operation of IQ generator and its calibration is explained in the following section. LO feedthrough can be introduced by the proposed downconverter due to the limited reverse isolation of g_m cell. However, the LO feedthrough does not affect to the normal PA or RX operation since the proposed impedance detection is duty-cycled operation. The impedance detection circuit only operates in the detection mode. Otherwise, in the normal PA or RX mode, it is disabled.

E. DTC-Based IQ Generator

Since a conventional quadrature-LO generation at the carrier frequency is too power hungry (~few mW) for just impedance detection and is not readily available from the sliding-IF structure, in this work, a dedicated ultra-low-power digital-to-time-converter (DTC) [19] based quadrature-LO generation with a relaxed noise performance is proposed, as shown in Fig. 9. The 2.4 GHz quadrature signals are generated by DTC, which comprises inverters and switchable capacitors. The delay of DTC can be controlled by digitally-controlled switchable capacitors. The DTC architecture is simple and consumes low power. However, the actual delay is sensitive to the accuracy of the capacitor value and process/voltage/temperature corners. To assure a 90° delay, a calibration scheme is further proposed, by comparing the outputs of the XOR and XNOR operations on the IQ signals. If the delay is less than 90°, the DC value of

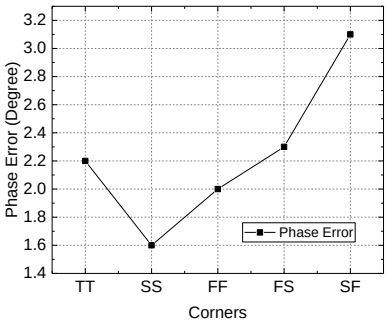

Fig. 12. Simulated IQ phase mismatch after calibration with process corners.

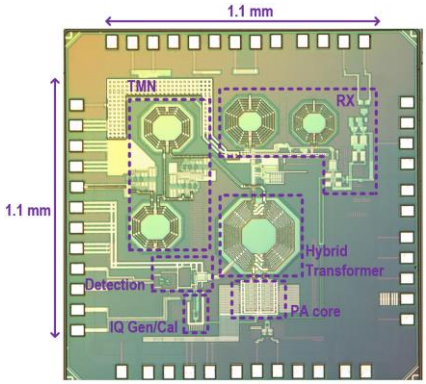

Fig. 13. Die Microphotograph.

XOR is less than that of XNOR, the case is vice versa if the delay is higher than 90°. When the delay is 90°, the DC values of XOR and XNOR are equal. The circuit block for the symmetrical XOR to minimize input phase offset is shown in Fig. 10. The XNOR operation can be implemented by swapping differential Q inputs. Similar as in the down converter, switches are added to disable the XOR and XNOR to reduce current consumption after calibration.

The simulated DC values of XOR and XNOR and quadrature phase difference values versus the delay code are shown in Fig. 11. Fig. 12 illustrates the simulated IQ phase mismatch after calibration over process variation. The maximum IQ phase mismatch is only 3.1°.

F. Low-Power Front-End Module

To verify the detection technique, the TMN is integrated with a low-power front-end module, including a 2.4GHz differential Class-D PA [20] and a sliding-IF RX. The class-D topology has higher efficiency by switching-mode operation [21]. Compared to class-E, its impedance matching network is easier to design. Note that the matching network is also necessary to suppress the harmonics from the switching PA. To share the TMN, the same optimum load/source impedance is designed for the PA/LNA, and a fixed matching network at the LNA input is used to match to a higher impedance.

IV. Measurement Results

The chip is fabricated in 40-nm CMOS, occupying a core area of 1.1×1.1mm^2 as shown in Fig. 13. The power

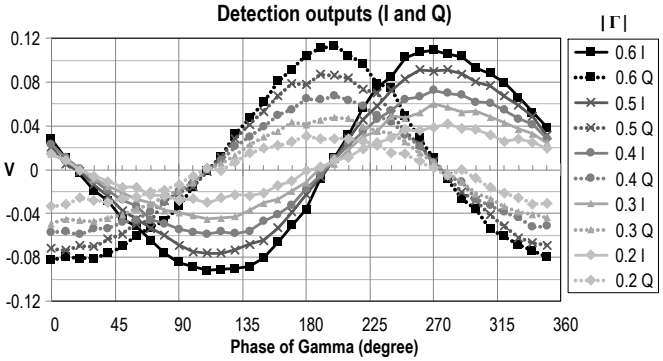

(a)

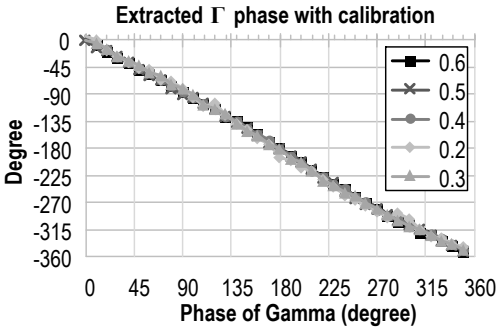

(b)

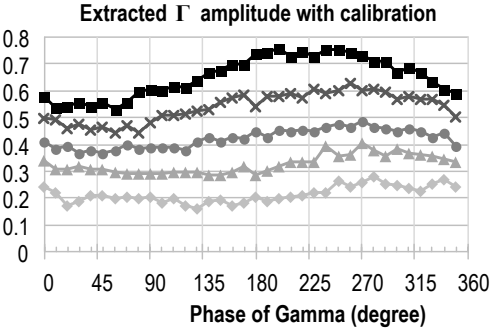

(c)

Fig. 14. Measured (a) impedance detection outputs, (b) extracted phase and (c) amplitude information

consumption of the detection is only 0.83 mW (including 0.6mW for the IQ generation and its buffering). A source/load impedance tuner is used to verify the impedance detection and characterize the RX and PA performance in case of impedance variation. The impedance tuning method can be explained as follows. First, the impedance calibration is implemented with a known Z_{cal} (150Ω in this work) and a default TMN setting. As a result, $\overrightarrow{F_{Cal}}$ in (14) is achieved. The detected antenna reflection coefficient in the first step after the impedance calibration described in Section II, $\overrightarrow{\Gamma_{Det1}}$, is calculated from (15) with the known $\overrightarrow{F_{Cal}}$. Note that the $\overrightarrow{F_{Cal}}$ also calibrates the PVT variation. Moreover, the impedance of the default TMN setting, $Z_{TMN,default}$, is also calculated as

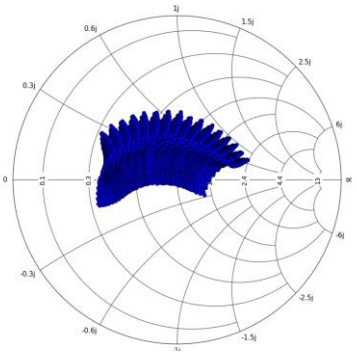

Fig. 15. Measured S_{11} tuning range of TMN.

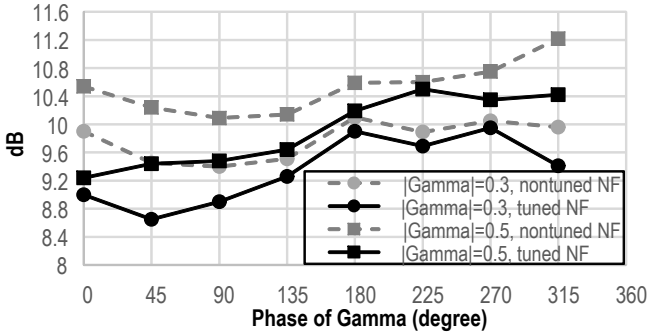

Fig. 16. Measured RX noise figure with and without tuning.

$$Z_{TMN,default} = \left(\frac{1+\overrightarrow{\Gamma_{Det1}}}{1-\overrightarrow{\Gamma_{Det1}}}\right)\cdot Z_{Cal} \qquad (17).$$

Second, after the calibration process, the antenna impedance, $Z_{Ant,}$ is also achieved with known $Z_{TMN,default}$ as

$$Z_{Ant} = \left(\frac{1-\overrightarrow{\Gamma_{Det2}}}{1+\overrightarrow{\Gamma_{Det2}}}\right)\cdot Z_{TMN,default} \qquad (18),$$

where $\overrightarrow{\Gamma_{Det2}}$ is the detected antenna reflection coefficient in the second step.

Finally, the impedance of TMN by optimum setting, $Z_{TMN,optimum}$ is obtained as

$$Z_{TMN,optimum} = \left(\frac{1+\overrightarrow{\Gamma_{Ant,optimum}}}{1-\overrightarrow{\Gamma_{Ant,optimum}}}\right)\cdot Z_{Ant} = Z^{*}_{Ant} \qquad (19),$$

where $\overrightarrow{\Gamma_{Ant,optimum}}$ is the antenna reflection coefficient to achieve $Z_{TMN,optimum}$. Those values can be also organized in a LUT. Therefore, the single-step tuning can be realized.

Fig. 14 shows the measured I and Q levels for different Γ_{Ant} (a), the calibrated phase (b) and amplitude of Γ_{Det} (c). The raw IQ levels result in a phase error of about 190° and the amplitudes are not directly linked to the $|\Gamma_{Ant}|$. After calibration, the phase of Γ_{Det} corresponds to the phase of the actual Γ_{Ant}, and is not dependent to $|\Gamma_{Ant}|$, as shown in Fig. 14(b). The detection phase is significantly improved after calibration with a worst-case error of about 18°, which is sufficient for the impedance tuning. One of the main contributors to the accuracy as 18º is coupling. By virtue of on-chip TMN integration, various

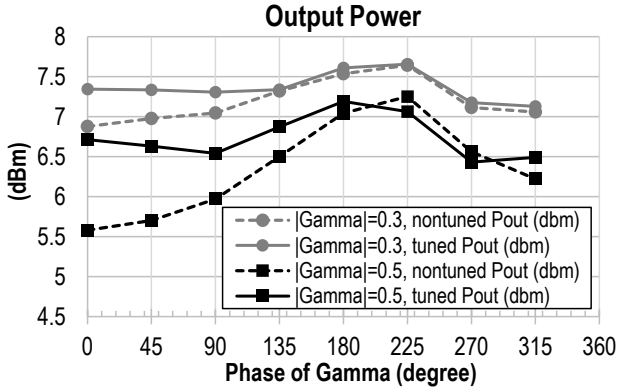

(a)

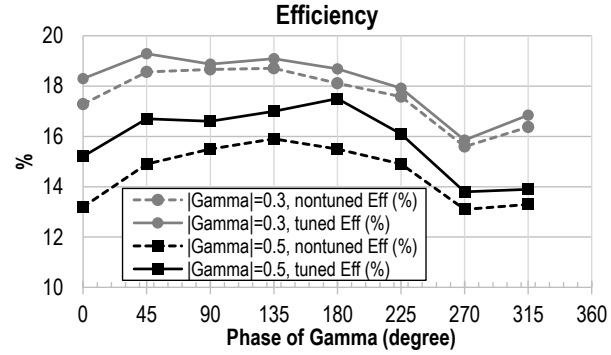

(b)

Fig. 17. Measured PA performance. (a) output power with and without tuning and (b) efficiency with and without tuning.

TABLE II
PERFORMANCE SUMMARY AND COMPARISON OF THE MISMATCH DETECTION AND TUNING SYSTEMS

	[3] ISSCC2009	[5] JSSC2014	[6] JSSC2014	This work
Detection method	Magnitude only	Magnitude only	Polar using weak coupling	Polar using Hybrid Transformer
Tunable matching purpose	Return loss	TX power and efficiency	TX power and efficiency	TX power and efficiency, RX NF
$\|\Gamma\|$ Tuning range	-	0.3	0.7	0.5
Optimization method	Exhaustive search	Exhaustive search	Successive Approximation	
Technology	0.18µm CMOS	0.18µm CMOS	0.13µm CMOS + SOI	40nm CMOS
Integration				
Mismatch detection:	on-chip	on-chip	on-chip	on-chip
Tuner:	off-chip	on-chip	off-chip	on-chip
Power consumption	31 mW	-	30 mW	0.83 mW 0.6 mW (IQ Gen) 0.23 mW (Det.)

couplings, e. g. L-to-L coupling among transformer and inductors and C coupling in inter transformer can affect to the accuracy compared to the off-chip matching. The calibrated $|\Gamma_{Det}|$ shows a good accuracy with an error of about 0.1 up to $|\Gamma_{Ant}|$ of 0.5. Based on the detected impedance, an optimum TMN setting is applied for the RX and PA. The measured S_{11} tuning range of the TMN in the smith chart is shown in Fig. 15. The S_{11} result can be also regarded as the conjugate S_{11} range of Z_{Ant} (Z^{*}_{Ant}) to match Z_{Ant}. The resulted noise figure (NF) of the RX is illustrated in Fig. 16, in comparison with the non-tuned case (with TMN setting for 50Ω matching). The NF is improved up to 0.9dB and 1.3dB for $|\Gamma_{Ant}|$ of 0.3 and 0.5.

Marginal improvement of the NF is noticed for Γ_{Ant} phase larger than 180°, which can be further improved by increasing the tuning range of the TMN. The output power and the efficiency, η, of the PA are shown in Fig. 17, in comparison with the non-tuned case (with TMN setting for 50Ω matching). The output power is improved up to 0.5dB and 1.2dB for $|\Gamma_{Ant}|$ of 0.3 and 0.5 respectively, while there is an overall improvement on η. Performance summary and comparison are shown in Table II.

V. Conclusion

This paper presents a novel impedance detection technique to compensate for the antenna impedance mismatch implemented in 40-nm CMOS process. The impedance mismatch is detected as the leakage signal due to the mismatch between actual antenna impedance and the reference impedance, via a hybrid transformer. The transformer serves both as the detection circuit and balun to convert from differential PA output to single-ended, is therefore area-efficient. Moreover, the impedance detection also has the phase information, which can be utilized to derive the complex antenna impedance. The complex impedance detection can realize single-step TMN tuning. A calibration scheme is implemented to improve the detection accuracy from 190º to 18 º, which is sufficient for impedance tuning. The detection circuit is co-designed together with the on-chip TMN to optimize the matching to cover impedance variation. It only dissipates 0.83 mW and no more power consumption is required after single-step impedance tuning. The TMN can cover Γ_{Ant} up to 0.5 with the proposed impedance detection technique in the ISM 2.4-GHz band. After the single-step impedance tuning, the PA power and RX NF are improved by up to 1.2 dB and 1.3 dB, respectively. Using the proposed schemes, the fully integrated TMN is allowable for ULP wearable/implantable devices.

References

[1] V. P. Rachin and W.-Y. Chung, " Wearable noncontact armband for mobile ECG monitoring system," *IEEE Trans. Biomed. Circuits Syst.*, vol.10, no. 6, pp. 1112-1118, Dec. 2016.

[2] R. Fontana, F. Mulana, C. Cavallotti, G. Tortora, M. Vigliar, M. Vatteroni, and A. Menciassi, " An innovative wireless endoscopic capsule with spherical shape," *IEEE Trans. Biomed. Circuits Syst.*, vol.11, no. 1, pp. 143-152, Feb. 2017.

[3] K. Boyle, Y. Yuan, and L. Ligthart, "Analysis of mobile phone antenna impedance variations with user proximity," *IEEE Trans. Antennas Propag.*, vol. 55, no. 2, pp. 364–372, Feb. 2007.

[4] J. de Mingo, A. Valdovinos, A. Crespo, D. Navarro, and P. Garcia, "An RF electronically controlled impedance tuning network design and its application to an antenna input impedance automatic matching system," *IEEE Trans. Microw. Theory Techn.*, vol. 52, no. 2, pp. 489–497, Feb. 2004.

[5] H. Song, B. Bakkaloglu, and J. T. Aberle, "A CMOS adaptive antenna-impedance-tuning IC operating in the 850MHz-to-2GHz band," in *Int. Solid-State Circuits Conf. (ISSCC) Dig. Tech Papers*, 2009, pp. 384-385,385a.

[6] S. M. Bowers, K. Sengupta, K. Dasgupta, and A. Hajimiri, "A fully integrated self-healing power amplifier," in *IEEE RFIC Symp. Dig.*, Jun. 2012, pp. 221–224.

[7] Y. Yoon, H. Kim, H. Kim, K.-S. Lee, C.-H. Lee, and J. S. Kenney, "A 2.4-GHz CMOS power amplifier with an integrated antenna impedance mismatch correction system," *IEEE J. Solid-State Circuits*, vol.49, no. 3, pp. 608-621, Mar. 2014.

[8] S. Kousai, K. Onizuka, J Wadatsumi, T. Yamaguchi, Y. Kuriyama, and M. Nagaoka, "Polar antenna impedance detection and tuning for efficiency improvement in a 3G/4G CMOS Power Amplifier," *IEEE J. Solid-State Circuits*, vol.49, no. 12, pp. 2902-2914, Dec. 2014.

[9] E.-L. Firrao, A.-J. Annema, and B. Nauta, "An automatic antenna tuning system using only RF signal amplitudes," *IEEE Trans. Circuits Syst. II*, vol.55, no. 9, pp. 833-837, Sep. 2008.

[10] P. Sjöblom, and H. Sjöland, "An adaptive impedance tuning CMOS circuit for ISM 2.4-GHz band," *IEEE Trans. Circuits Syst. I*, vol.52, no. 9, pp. 1115-1124, Jun. 2005.

[11] C. Lu, A. Ba, Y.-H. Liu, X. Wang, C. Bachmann, and K. Philips, "A sub-mW antenna-impedance detection using electrical balance for single-step on-chip tunable matching in wearable/implantable applications," in *Int. Solid-State Circuits Conf. (ISSCC) Dig. Tech Papers*, 2017, pp. 298-299.

[12] E. Roverato, M. Kosunen, K. Cornelissens, S. Vatti, P. Stynen, K. Bertrand, T. Korhonen, H. Samsom, P Vandenameele, J. Ryynänen, " All-digital RF transmitter in 28nm CMOS with programmable RX-band noise shaping," in *Int. Solid-State Circuits Conf. (ISSCC) Dig. Tech Papers*, 2017, pp. 222-223.

[13] P. Madoglio, H. Xu, K. Chandrashekar, L. Cuellar, M. Faisal, W. Y. Li, H. S. Kim, K. M. Nguyen, Y. Tan, B. Carlton, V. Vaidya, Y. Wang, T. Tetzlaff, S. Suzuki, A. Fahim, P. Seddighrad, J. Xie, Z. Zhang, D. S. Vemparala, A. Ravi, S. Pellerano, and Y. Palaskas, " A 2.4GHz WLAN digital polar transmitter with synthesized digital-to-time converter in 14nm Trigate/FinFET technology for IoT and wearable applications," in *Int. Solid-State Circuits Conf. (ISSCC) Dig. Tech Papers*, 2017, pp. 226-227.

[14] Y. H. Chee, F. Golcuk, T. Matsuura, C. Beale, J. F. Wang, and O. Shanaa, "A digitally assisted CMOS WiFi 802.11ac/11ax front-end module achieving 12% PA efficiency at 20dBm output power with 160MHz 256-QAM OFDM signal," in *Int. Solid-State Circuits Conf. (ISSCC) Dig. Tech Papers*, 2017, pp. 292-293.

[15] E. Sartori, "Hybrid transformers," *IEEE Trans. Parts, Mater., Packag.*, vol. PMP-4, no. 8, pp. 59–66, Sep. 1968.

[16] M. Mikhemar, H. Darabi, and A. Abidi, "A tunable integrated duplexer with 50dB isolation in 40nm CMOS," in *Int. Solid-State Circuits Conf. (ISSCC) Dig. Tech Papers*, 2009, pp. 386-387.

[17] S. H. Abdelhalem, P. S. Gudem, and L. E. Larson "Hybrid transformer-based tunable differential duplexer in a 90-nm CMOS Process," *IEEE Trans. Microw. Theory Tech.*, vol. 61, no. 3, pp. 1316-1326, Mar. 2013.

[18] S. H. Abdelhalem, P. S. Gudem, and L. E. Larson "Tunable CMOS integrated du plexer with antenna impedance tracking and high isolation in the transmit and receive bands," *IEEE Trans. Microw. Theory Tech.*, vol. 62, no. 9, pp. 2092-2104, Sep. 2014.

[19] Y.-H. Liu, J. van den Heuvel, T. Kuramochi, B. Büsze, P. Mateman, V. K. Chillara, B. Wang, R. B. Staszewslki, and K. Philips, "An ultra-low power 1.7-2.7 GHz fractional-*N* sub-sampling digital frequency synthesizer and modulator for IoT applications in 40 nm CMOS," *IEEE Trans. Circuits Syst. I*, vol.64, no. 5, pp. 1094-1105, May 2017.

[20] A. Ba, V. K. Chillara, Y.-H. Liu, H. Kato, K. Philips, and R. B. Staszewski, "A 2.4GHz class-D power amplifier with conduction angle calibration for -50dBc harmonic emissions," in *Proc. IEEE Radio Frequency Integrated Circuits (RFIC) Symp.*, 2014, pp. 239-242.

[21] S.-M. Yoo, J. S. Walling E. C. Woo, B. Jann, and D. J. Allstot, "A switched-capacitor RF power amplifier," *IEEE J. Solid-State Circuits*, vol.46, no. 12, pp. 2977-2987, Dec. 2011.

Minyoung Song (S'06–M'11) received the B.S. and Ph. D. degree in electrical engineering from Korea University, Seoul, Korea, in 2006 and 2013, respectively. He has been with the Holst Centre/imec, Eindhoven, the Netherlands, since 2016, where he is currently a Researcher. He was a Senior Engineer with Samsung Electronics, Hwaseong, from 2013 to 2016. He was a visiting scholar with the University of California, Los Angeles, from 2008 to 2009. He was also a Visiting Scholar with the University of California, Santa Cruz, 2012. His current research interests are energy-

efficient digitally-assisted RFIC, frequency synthesizers/clock generators and high-speed wireline transceivers. Dr. Song was a recipient of the IEEE Seoul Section Student Paper Contest Bronze Award in 2007 and 2010.

Chuang Lu was born in Chengwu, China in 1986. He received the B.Sc. degree from the Zhejiang University, Hangzhou, China, in 2008, and the M.Sc. degree from the Eindhoven University of Technology, Eindhoven, the Netherlands, in 2010. In 2015, he received the Ph.D. degree from the Mixed-Signal Microelectronics Group, Eindhoven University of Technology.
In 2009, he was with Philips Research, Eindhoven, the Netherlands, as an intern. In 2012, he was with Catena Microelectronics, B.V., Delft, the Netherlands, as an exchange researcher. From 2014 to 2016, he worked in IMEC-Holst Centre, Eindhoven, the Netherlands. Since December 2016, he has been working in NXP, Eindhoven, the Netherlands, as millimeter-wave design engineer.

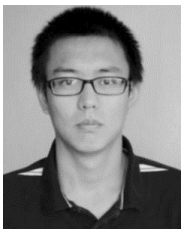

Ao Ba received the B.E. degree in microelectronics from Sun Yat-Sen University, Guangzhou, China, in 2009, and the M.S. degree (cum laude) in electrical engineering from Delft University of Technology, Delft, the Netherlands, in 2011. In 2011, he joined Holst Centre/imec, the Netherlands, as a researcher. His technical interests include ultra-low power RF and mixed-signal IC design and digitally-assisted RF IC design.

Xiaoyan Wang received her M.S. and Ph.D degrees from National University of Singapore in 2002 and Technical University of Denmark in 2004, respectively. She has been working with Huawei Technologies in China, Infineon Technologies in Germany and Institute of Microelectronics in Singapore from 1997 to 2008. Since 2008, she works with Holst Centre/imec as a senior researcher and her current research interest is ultra-low-power transceiver design for IoT platform.

Yao-Hong Liu (S'04-M'09) received his Ph.D. degree from National Taiwan University, Taiwan, in 2009.
Since 2010, he joined imec, the Netherlands. His current position is Principal Membership of Technical Staff, and he is leading the development of the ultra-low power (ULP) RFIC design. His research focuses is energy-efficient digital-intensive RF transceivers for IoT and sensing applications.
He currently serves as a technical program committee of IEEE ISSCC and RFIC symposium.

Kenichi Shibata was born in Nagano, Japan, in 1982. He received the B.S. and M.S. degrees in electrical engineering from Gunma University, Gunma, Japan, in 2006 and 2008, respectively.
He joined Renesas Technology Corporation, Gunma, Japan, in 2008. Since 2010, he has been involved in development of low-cost and low-power RF transceiver.
He is currently a Senior Staff Engineer of the RF Solution Department, Industrial Analog and Power Business Division with Renesas Electronics Corporation, Tokyo, Japan.
From 2016, he is also an industrial resident of the research program in Holst Center/imec.

Christian Bachmann is program manager of imec's ULP Wireless Systems program. He joined imec in 2011, working on ultra-low-power wireless communication systems, digital baseband processing, and hardware/software co-design. In his previous work he has covered various wireless communication solutions for 802.11ah WiFi, Bluetooth LE, 802.15.4 (Zigbee), ultra-wideband impulse radio and others. Prior to joining imec, he has been researching hardware-accelerated power estimation for VLSI systems both with Infineon Technologies and Graz University of Technology in Graz, Austria, receiving his PhD in Electrical Engineering in 2011.

Kathleen Philips is a program director at imec, in the area of Perceptive Systems for the IoT. Dr. Philips holds a PhD in Electrical engineering and has 20 years of experience in the domain of low power mixed-signal, RF and integrated system design. She started her career at Philips Research, The Netherlands, working an analog and mixed-signal circuits. She joined the Holst Centre/imec in 2007, where she is currently leading a program on ultra-low power wireless, processing and sensing systems. This is part of an open innovation collaboration, together with local and international industry. The research targets applications in the area of infrastructure and person-centric IoT systems, with a focus on ultra-low power communication and sensing.